Received 9 November 2022; revised 13 December 2022; accepted 17 December 2022. Date of publication 26 December 2022; date of current version 23 January 2023.

Digital Object Identifier 10.1109/OJAP.2022.3231885

Surface Electromagnetic Waves at Seawater-Air and Seawater-Seafloor Interfaces

IGOR I. SMOLYANINOV[1], QUIRINO BALZANO[2], AND ALEXANDER B. KOZYREV[3]

[1]Saltenna LLC, McLean, VA 22102, USA
[2]ECE Department, University of Maryland at College Park, College Park, MD 20740, USA
[3]Collins Aerospace, Cedar Rapids, IA 52402, USA

CORRESPONDING AUTHOR: I. I. SMOLYANINOV (e-mail: igor.smolyaninov@saltenna.com)

This work was supported by DARPA and AFRL under Award FA8650-20-C-7027.

ABSTRACT Underwater radio communication using surface electromagnetic waves propagating along the seawater-air and seawater-sea floor interfaces may provide a promising alternative to commonly used acoustic communication underwater. Here we present a detailed analytical and numerical consideration of TE and TM polarized surface electromagnetic wave properties. The resulting surface waves have propagation constants that permit communication ranges far longer than those of bulk propagation in the lossy media. We demonstrate theoretically and experimentally their ability to carry broadband radio signals over practical communication distances underwater. A 50 MHz radio signal was successfully carried along the sandy seabed over 7 m distance.

INDEX TERMS Propagation length, seawater, surface electromagnetic wave, underwater radio communication.

I. INTRODUCTION

WIDE band communication underwater is required in many applications, such as command and control of manned and unmanned underwater vehicles, networked underwater sensors, etc. However, the bandwidth of acoustic communication underwater is limited due to slow propagation speeds and multipath effects. Conventional radio frequency signals have severely limited communication range due to rapid attenuation in seawater [1], [2], [3], while directional optical links need sophisticated pointing, acquisition and tracking, and water turbidity strongly affects their performance. As a result, underwater wireless communication remains a critical problem that needs a viable solution.

Very recently we have reported a design of a surface electromagnetic wave (SEW) radio antenna, which operates in the 2.4 GHz band and which efficiently launches surface electromagnetic waves along an interface between a conductor and a dielectric [4]. The antenna operation is based on strong field enhancement at the antenna tip, and it was demonstrated that this antenna may be used to send broadband radio communication signals through conductive enclosures, such as a commercial Faraday cage. A successful adaptation of this surface wave antenna design for underwater radio communication was reported in [5]. This antenna operated in the 50 MHz band and it was able to launch SEWs along the seawater-air interface. Since the propagation length of SEW along the interface considerably exceeds the skin depth of radio waves at the same frequency, the surface wave technique may be used for underwater broadband wireless communication over practical distances. A typical geometry of such SEW radio system consists of two conventional radios equipped with SEW antennas and positioned near a surface wave-carrying interface.

Given the potential practical importance of SEW solutions of Maxwell equations at the seawater-air interface, and limited literature on SEW properties in this geometry, it is important to develop a detailed theoretical consideration of surface electromagnetic wave properties and demonstrate their ability to carry broadband radio signals over practical communication distances underwater. Compared to the previous studies reported in [4], [5], where only the properties of TM waves were studied, we also need to examine the TE-polarized solutions, so that the best SEW antenna configuration may be chosen for a given application. In addition, since interfaces other than air-water may also be

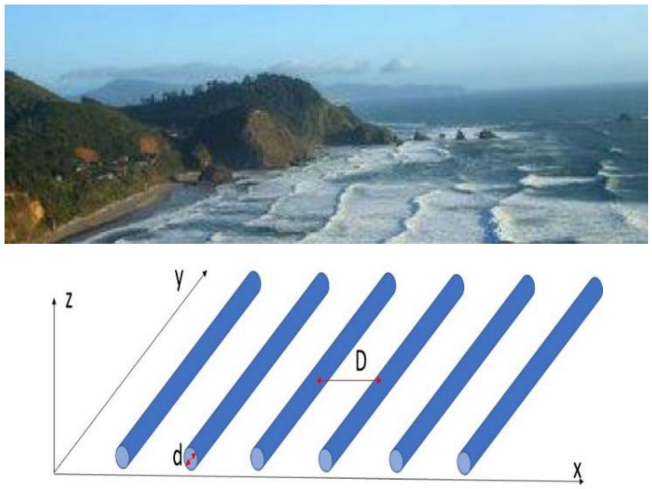

FIGURE 1. The interfacial layer of wavy seawater is modeled as an array of cylinders having the dielectric properties of seawater.

present in communication geometries of practical importance, it is important to determine if other interfaces, such as the seawater-sea floor interface may also be used for RF communication underwater. These important tasks provide motivation for our study.

II. METHODS AND PROCEDURES

A. GENERAL THEORETICAL FRAMEWORK

Let us review solutions of the macroscopic Maxwell equations in a non-magnetic ($\mu_r = 1$) medium having continuous dielectric permittivity $\varepsilon(z)$, which depends only on z coordinate. Such an assumption was made because we are interested in dealing with the electromagnetic wave propagation along sandy seafloors and at the air/sea surface interface. In both cases the interface between the two media presents a dielectric property variation mostly along the vertical direction over a substantial area of the sea surface. Assuming time harmonic field dependencies proportional to $e^{-i\omega t}$, the macroscopic Maxwell equations are:

$$\vec{\nabla}\cdot\vec{D} = \rho,\ \vec{\nabla}\cdot\vec{B} = 0,\ \vec{\nabla}\times\vec{E} = i\omega\vec{B}\text{, and}$$
$$\vec{\nabla}\times\vec{H} = \vec{J} - i\omega\vec{D} \tag{1}$$

Straightforward transformations of Eq. (1) lead to a wave equation:

$$\vec{\nabla}\times\left(\vec{\nabla}\times\vec{E}\right) - \frac{\omega^2\varepsilon}{c^2}\vec{E} = i\omega\mu_0\vec{J} \tag{2}$$

Following further transformations, it may be recast as

$$-\nabla^2\vec{E} - \vec{\nabla}\left(E_z\frac{\partial\varepsilon}{\varepsilon\partial z} - \frac{\rho}{\varepsilon}\right) - \frac{\varepsilon\omega^2}{c^2}\vec{E} = i\omega\mu_0\vec{J} \tag{3}$$

Since the electromagnetic far-field generated by a source may be obtained as a superposition of source-free modes propagating away from the source, we are interested in the source-free ($\rho = 0$ and $J = 0$) solutions of Eq. (3). Without a loss of generality, we may search for source-free surface mode solutions propagating in the x direction as $e^{i(kx-\omega t)}$. This way, a vector problem could be reduced to a two-dimensional scalar one. For both polarization states (TE or TM) Eq. (3) may be recast as an effective one-dimensional Schrödinger equation:

$$-\frac{\partial^2 E_y}{\partial z^2} - \frac{\varepsilon(z)\omega^2}{c^2}E_y = -k^2E_y \tag{4}$$

in the case of TE polarization (in which $E_z = 0$), and as

$$-\frac{\partial^2 E_z}{\partial z^2} - \frac{\partial E_z}{\partial z}\frac{\partial \ln\varepsilon}{\partial z} - \left(\frac{\varepsilon(z)\omega^2}{c^2} + \frac{\partial^2 \ln\varepsilon}{\partial z^2}\right)E_z = -k^2E_z \tag{5}$$

in the case of TM polarization (in which $E_z \neq 0$). Furthermore, by making a $E_z = \psi/\varepsilon^{1/2}$ substitution, Eq. (5) may be recast as

$$-\frac{\partial^2\psi}{\partial z^2} + \left(-\frac{\varepsilon(z)\omega^2}{c^2} - \frac{1}{2}\frac{\partial^2\varepsilon}{\varepsilon\partial z^2} + \frac{3}{4}\frac{(\partial\varepsilon/\partial z)^2}{\varepsilon^2}\right)\psi$$
$$= -\frac{\partial^2\psi}{\partial z^2} + V\psi = -k^2\psi \tag{6}$$

where ψ is the new "wave function" for the TM polarized wave. In both Eq. (4) and Eq. (6) the role of energy is played by the $-k^2$ term. On the other hand, the expressions for the effective potentials are different for the TE and TM polarizations. In the case of TE polarization the effective potential energy equals $V(z) = -\varepsilon(z)\omega^2/c^2$. Therefore, solutions of Eq. (4) may only have a propagating character ($\mathrm{Im}(k) \ll \mathrm{Re}(k)$) if $\varepsilon(z)$ is positive and almost real (so that the $\varepsilon(z)$ distribution looks like a dielectric waveguide). On the other hand, SEW solutions do appear in the TM case due to the presence of derivative terms in the effective potential energy. Before analyzing solutions of Eqs. (4, 6) for the seawater-air interface, we need to consider detailed $\varepsilon(z)$ profiles at the interface as a function of RF frequency.

B. PROFILE OF THE DIELECTRIC PERMITTIVITY $\varepsilon(Z)$ NEAR THE SEAWATER-AIR INTERFACE

The seawater surface is typically perturbed by waves, whose frequency spectrum and amplitude are well studied, and which are driven by winds blowing along the sea surface (see Fig. 1). The electromagnetic properties of this transition layer between the bulk seawater and air are not well studied. We need to understand these properties to accurately predict the basic characteristics of the surface electromagnetic waves propagating along the interface, such as their propagation length and penetration depth into the bulk seawater and air. The derived interfacial properties may be used to deduce the frequency-dependent effective $\varepsilon(z)$ profile, which may be plugged into Eqs. (4, 6). Within the scope of our simplified model, we have assumed that the transition layer is composed of parallel cylinders (see Fig. 1), whose dielectric permittivity coincides with the permittivity of seawater. The distance D between these cylinders and the cylinder diameters d are assumed to coincide with the period and height of the waves at a given wind speed. Depending on

the ratio of the wave period D to the free space wavelength of the electromagnetic waves λ_0, we can model the transition layer properties using either photonic crystal or metamaterial tools. Since the typical wavelength of wind waves is 60-150 m, the metamaterial properties dominate in the ELF and VLF ranges, while the photonic crystal model should be more appropriate in the MHz range. On the other hand, near shore the ocean wave pattern typically becomes much more chaotic and aperiodic. The electromagnetic properties of such a chaotic transition layer may be described using the Maxwell-Garnett approximation, which typically works well in the description of effective medium properties of random mixtures.

In the limit $\lambda_0 >> D$, the interfacial seawater surface layer of thickness d depicted in Fig. 1 may be described using the well-known metamaterial approximation for a uniaxial medium (see for example [6]). In this limit the diagonal components of the dielectric permittivity tensor of the surface layer are given as

$$\varepsilon_1 = \varepsilon_{x,z} = \frac{2\alpha\varepsilon_m\varepsilon_d + (1-\alpha)\varepsilon_d(\varepsilon_d+\varepsilon_m)}{(1-\alpha)(\varepsilon_d+\varepsilon_m)+2\alpha\varepsilon_d} \approx 1+2\alpha \quad (7)$$

$$\varepsilon_2 = \varepsilon_y = \alpha\varepsilon_m + (1-\alpha)\varepsilon_d \approx \alpha\varepsilon_m \quad (8)$$

where α is the volume fraction of water, and ε_m and ε_d are the dielectric permittivities of water and air, respectively. In the low frequency ranges of interest, the dielectric permittivity of seawater is typically assumed to be defined by its conductivity $\sigma = 4$ S/m:

$$\varepsilon_{water} = \varepsilon_m \approx i\varepsilon_m'' = \frac{i\sigma}{\varepsilon_0\omega} >> \varepsilon_m' \quad (9)$$

where ε_0 is the dielectric permittivity of vacuum [5] (however, recent experimental measurements by Midi et al. [7] cast some doubts on this assumption). Eqs. (7, 9) indicate that in the surface transition layer $\varepsilon_{x,z} > 1$ and almost purely real, which means that the wavy seawater surface may support a guided mode propagating in the y direction. A similar conclusion remains valid also for a chaotic wavy surface transition layer considered using the Maxwell-Garnett approximation. The isotropic electromagnetic properties of the interfacial seawater layer may be described by the well-known Maxwell-Garnett expression:

$$\left(\frac{\varepsilon_{eff}-\varepsilon_d}{\varepsilon_{eff}+2\varepsilon_d}\right) = \alpha\left(\frac{\varepsilon_m-\varepsilon_d}{\varepsilon_m+2\varepsilon_d}\right) \quad (10)$$

where ε_{eff} is the effective dielectric permittivity of the transition layer, $\varepsilon_d = 1$ is the dielectric permittivity of the "matrix" medium (air), ε_m is the dielectric permittivity of seawater considered as "inclusion", and α is the volume fraction of inclusions. The resulting expression for ε_{eff} is:

$$\varepsilon_{eff} = \varepsilon_d \frac{2\alpha(\varepsilon_m-\varepsilon_d)+\varepsilon_m+2\varepsilon_d}{2\varepsilon_d+\varepsilon_m-\alpha(\varepsilon_m-\varepsilon_d)} \quad (11)$$

In the limit of small α and $\varepsilon_d << \varepsilon_m$, the effective permittivity of the transition layer is $\varepsilon_{eff} = 1 + 3\alpha$ (note that it is almost purely real). The physical meaning of this result is that electric field of a propagating electromagnetic wave is "pushed out" of the high dielectric permittivity volumes occupied by "inclusions", leading to corresponding increase in ε_{eff}. We are going to use these expressions to approximate $\varepsilon(z)$ behavior near the seawater-air interface.

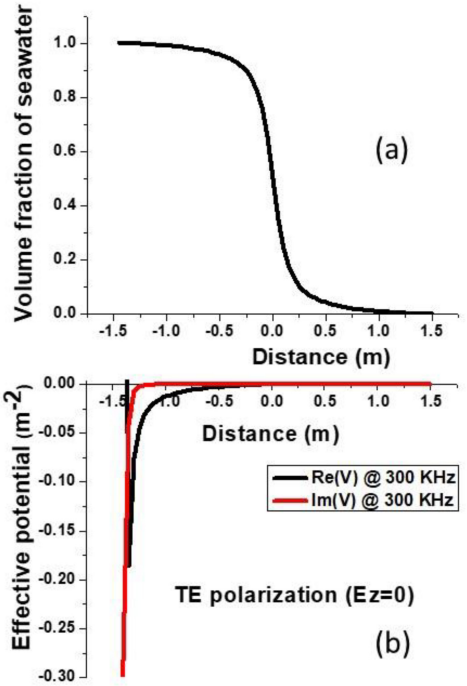

FIGURE 2. (a) Assumed volume fraction of seawater in the transition layer between bulk water and air. (b) Real and imaginary parts of the corresponding effective surface potential at 300 KHz.

III. RESULTS

A. ANALYTICAL STUDY OF THE TE AND TM GUIDED WAVES AT THE SEA SURFACE

Let us first concentrate on the properties of the TE waves ($E_z = 0$). For the TE polarization the effective Schrödinger equation is given by Eq. (4). The effective potential in Eq. (4) appears to be much less sensitive to the exact properties of the transition layer compared to the TM case (it depends only on $\varepsilon(z)$, but not on its derivatives), which may have advantages in some practical applications. As was revealed by Eqs. (7) and (11), the TE polarized wave experiences an attractive potential well near the wavy seawater-air interface. The plots of the assumed volume fraction of seawater α in the transition layer and the corresponding effective surface potential well for the TE wave calculated using Eq. (11) is presented in Fig. 2. We have verified that the effective potential energy behavior near the seawater-air interface appears to be rather insensitive to the magnitude of the real part of ε_{water}. Based on the Maxwell-Garnett approximation used in these calculations, the imaginary part of the effective potential appears to be large only very near the bulk seawater. Therefore, the TE guided wave defined by the effective potential shown in Fig. 2 is supposed to have a relatively long propagation range. We should also note that

the sharp increase in Im(V) near bulk seawater leads to very small electric field in the surface wave TE solutions, so that $E_y = 0$ condition may be assumed for these modes near bulk seawater. As a result, the bulk seawater boundary may be replaced by a ground plane in numerical simulations of these modes.

Let us now study analytical properties of Eq. (6) in the limit $\omega \to 0$, which is relevant in the HF and lower frequency ranges, by taking into account that $\varepsilon(z)$ in seawater has a very large imaginary part. In this limit Eq. (6) becomes

$$-\frac{\partial^2\psi}{\partial z^2} - \left(\frac{1}{2}\frac{\partial^2\varepsilon}{\varepsilon\partial z^2} - \frac{3}{4}\frac{(\partial\varepsilon/\partial z)^2}{\varepsilon^2}\right)\psi = -k^2\psi \qquad (12)$$

In the limit of very large ε the second term contribution to the effective potential may be neglected (since $\varepsilon^2 >> \varepsilon$), and we obtain the following 1D Schrödinger equation for the TM polarization:

$$-\frac{\partial^2\psi}{\partial z^2} - \frac{1}{2}\frac{\partial^2\varepsilon}{\varepsilon\partial z^2}\psi = -k^2\psi \qquad (13)$$

The effective potential energy (the second term in this equation), which is plotted in Fig. 3b, remains real even in the case of very large purely imaginary ε(z), which means that (similar to any other 1D Schrödinger equation) such a potential well will always have at least one bound state. Such a bound state will give rise to at least one solution having almost purely real longitudinal wave vector k, which corresponds to a surface mode with a long propagation length along the air/seawater boundary [8].

Let us also verify that this low frequency approximation remains valid at 300 KHz. The real and imaginary parts of the complete effective potential energy defined by Eq. (6) are plotted in Fig. 3c. It's low loss part appears to be similar to the potential shown in Fig. 3b, while the high loss region of the potential well (located in bulk seawater) is separated from the low loss region by a potential step. For a shallow potential well $V(z)$ the long propagating range eigenstate may be approximately determined as using the virial theorem [9] as

$$k^2 \approx \frac{\int_{-\infty}^{\infty}\psi V(z)\psi^* dz}{2\int_{-\infty}^{\infty}\psi\psi^* dz} \qquad (14)$$

(due to almost $\sim 1/z$ functional behavior of $V(z)$ near the potential barrier located in the vicinity of the bulk seawater, see Fig. 3b,c). Alternatively, the effective Schrödinger equation may be solved numerically using the Numerov [10] method. The numerically obtained effective energy level is shown schematically in green (hard to see) in Fig. 3(c). The wavelength of the resulting surface wave solution is $\lambda = 2\pi/k$, and $L = \mathrm{Im}(k)^{-1}$ defines the propagation distance of the wave. Note that the range of wave vectors k predicted by the application of Eq. (14) to the shape of the effective potential wells calculated in Figs. 3(b,c) differs drastically from the result predicted by the well-known expression for

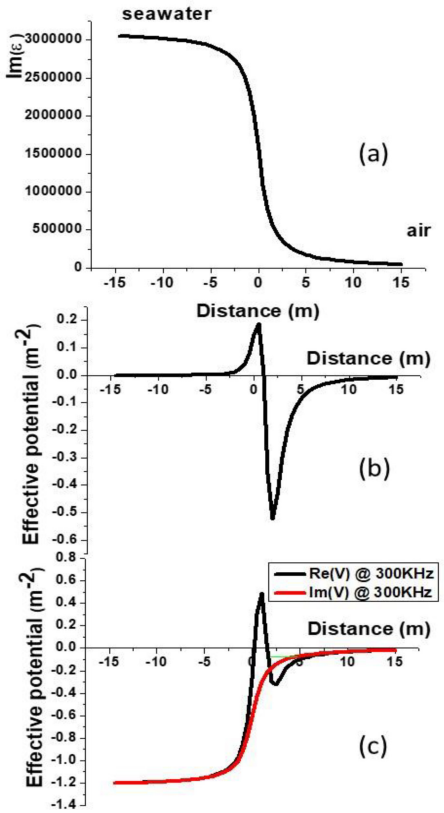

FIGURE 3. (a) Plot of $\varepsilon(z)$ in the transition layer wherein the dielectric permittivity changes from ε_{water} to ε_{air}. It is assumed that the water surface is wavy, and the typical wave height is ~ 5 m. (b) Effective potential energy near the air-seawater interface shown in (a) calculated for the 300 kHz frequency band using Eq. (13). (c) Complete effective potential energy defined by Eq. (6) (both real and imaginary parts) at the air-seawater interface plotted for the 300 KHz band for the same $\varepsilon(z)$ transition layer. The numerically obtained effective energy level is shown in green.

the k vector of the Zenneck wave [11], [12]:

$$k = \frac{\omega}{c}\left(\frac{\varepsilon_1\varepsilon_2}{\varepsilon_1 + \varepsilon_2}\right)^{1/2} \qquad (15)$$

where ε_1 and ε_2 are the dielectric permittivities of the neighboring media. Application of Eq. (15) to the case of a sharp planar seawater-air interface at $\nu = 300$ KHz produces $k \sim 2\pi\nu/c \sim 6.3\cdot 10^{-3}$ m^{-1}. On the other hand, the effective potential well shown in Fig. 3 together with Eq. (14) predict $k \sim 10^{-1}$ m^{-1}. This order of magnitude discrepancy indicates a distinctly different nature of the surface wave solution resulting from the calculations plotted in Fig. 3. However, small variations of the $\varepsilon(z)$ profile near the air-seawater interface depicted in Fig. 4 reveal an additional solution of Eq. (6), which is much more "Zenneck-like". It is clear that depending on the exact profile of $\varepsilon(z)$, the $3(d\varepsilon/dz)^2/(4\varepsilon^2)$ term of the effective potential in Eq. (6) may start to dominate at the very top region of the transition layer, which leads to appearance of a second, more shallow potential well. Application of Eq. (15) to the case of a planar sharp seawater-air interface at $\nu = 10$ MHz produces $k \sim 2\pi\nu/c \sim 0.21$ m^{-1}, which is very close to the estimate based on Eq. (14) for the second, more shallow potential well in Fig. 4. Thus, our

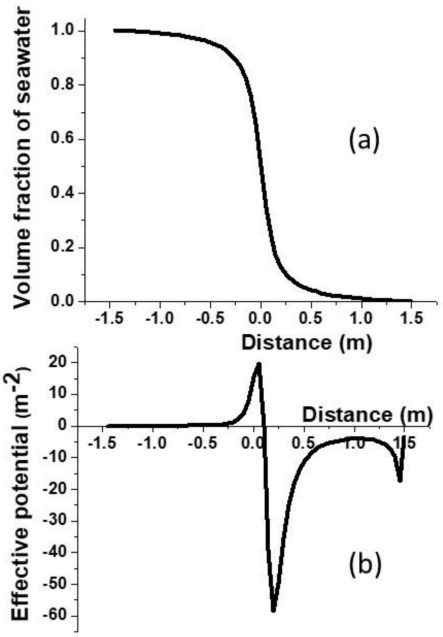

FIGURE 4. Effective potential energy near the air-seawater interface (b) calculated for the 10 MHz frequency band using Eq. (6) for a ∼0.5 m wavy transition layer (shown in (a)) between air and seawater. The second more shallow potential well at the very top edge of the transition layer gives rise to a Zenneck-like solution of Eq. (6).

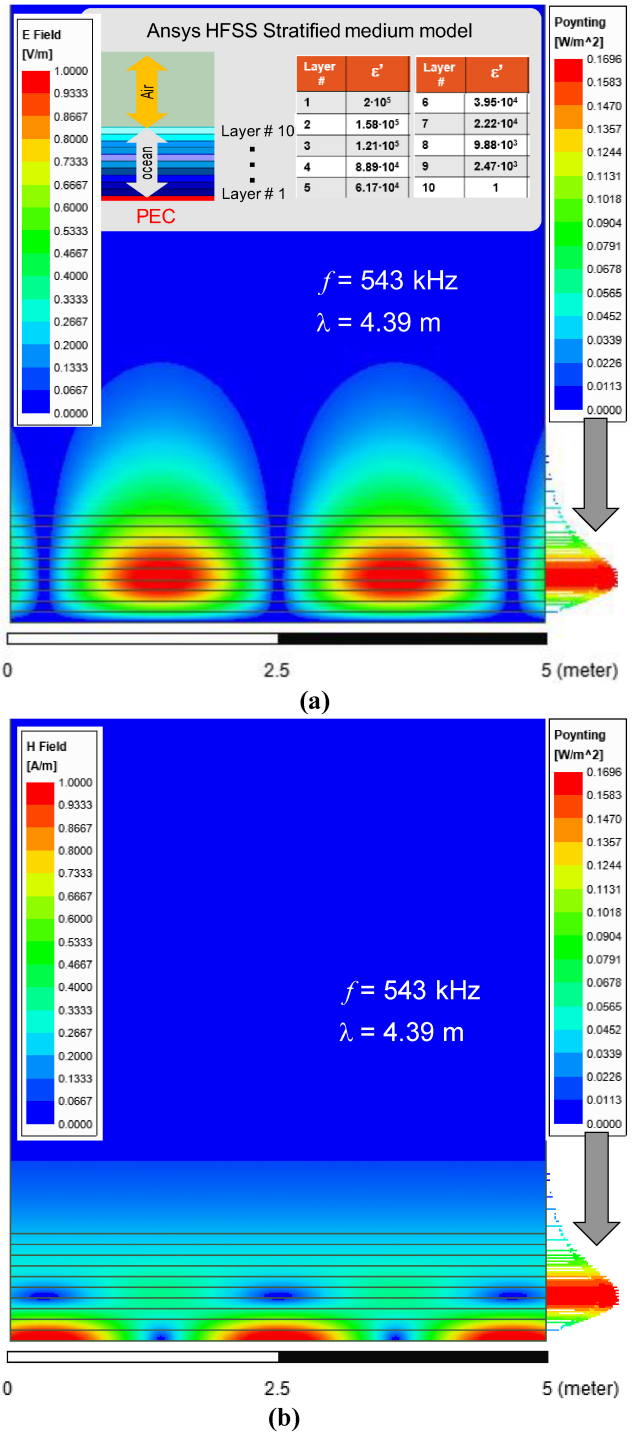

FIGURE 5. Electric (a) and magnetic (b) field distribution in the surface TE mode at 543 kHz and wavelength of 4.39 m. The arrows on the right show spatial distribution of the magnitude of the Poynting vector for this mode. The inset in (a) shows the details of the HFSS model used in simulations. The stratified medium has been modeled with 10 layers of dielectric medium. Each layer is 10 cm thick. The values of the real part of the dielectric constant in each layer are specified in the table. The conductivity of the bulk sea water was assumed to be 5 S/m and the conductivity of the layers was scaled following the same law as the real part of dielectric constant.

theoretical approach successfully recovers the conventional Zenneck wave solutions, while revealing additional propagating surface electromagnetic waves, which appear when the medium conductivity experiences gradual change across an interface.

B. NUMERICAL SIMULATIONS OF TE AND TM SURFACE WAVE PROPERTIES AT THE SEAWATER-AIR INTERFACE

The properties of surface waves discussed above have been also simulated using Ansys HFSS eigenmode solver. The solver calculates a set of resonance frequencies together with corresponding field distributions for a given phase shift at the boundaries. This phase shift defines the wavelength of the propagating surface mode for corresponding resonant frequency. We used two models of seawater-air interface, namely, a stratified model and a periodic model. In the stratified model we assumed that the chaotic waves at the air-ocean interface lead to the medium with dielectric constant changing with vertical coordinate z. This stratified medium has been modeled in HFSS as a multilayer dielectric structure. In our simulations we used 10 layers having thickness of 10 cm each. Details of this model are presented at the inset in Fig. 5(a). Here we used the value of the dielectric constant of bulk seawater presented in [7]. These experimental data are different from the conventional values in the literature where it is usually assumed that, in ELF to low MHz range, the imaginary part of the dielectric constant of sea water is defined by the seawater conductivity (about 5 S/m), and its real part is $\varepsilon' \sim 81$. To investigate the effect of the real part of seawater dielectric permittivity on the SEW structure, we also performed simulations of the SEW structure for conventional value of the dielectric constant of bulk seawater. It appears that these simulation

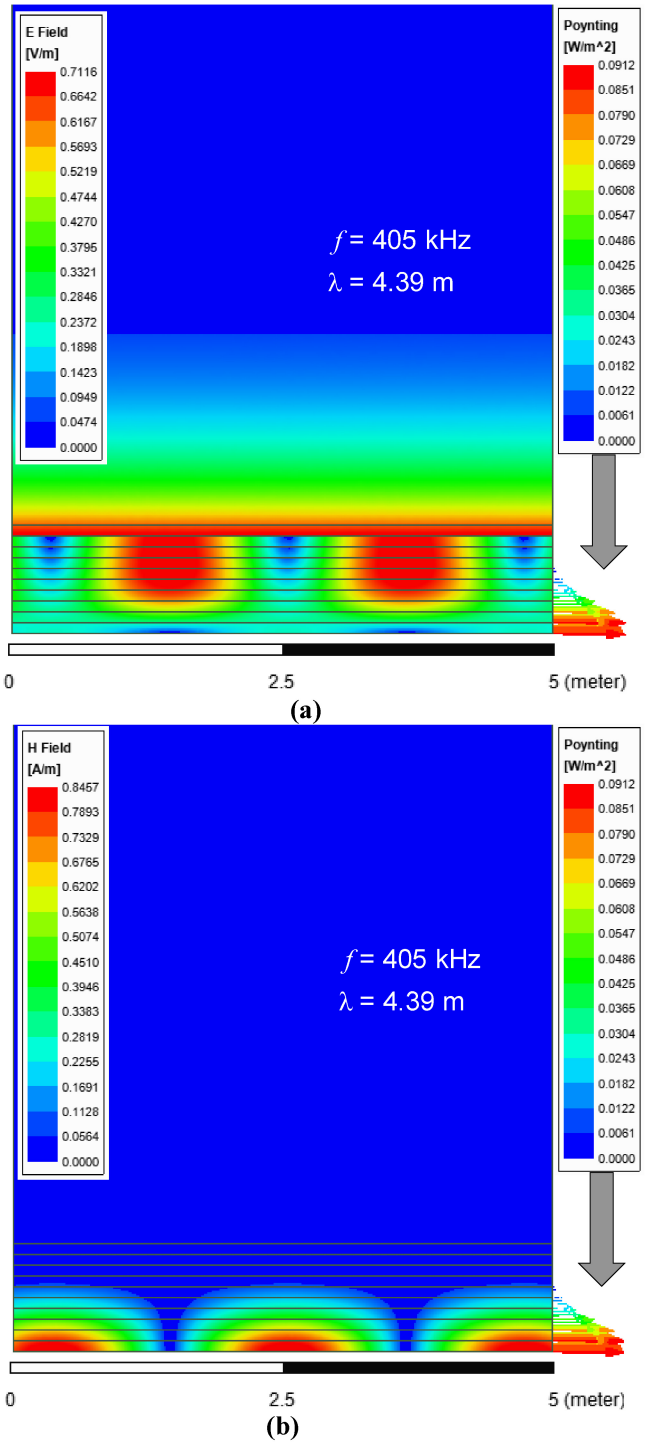

FIGURE 6. Electric (a) and magnetic (b) field distribution in the surface TM mode at 405 kHz and wavelength of 4.39 m, simulated using stratified medium model specified at the inset to Fig. 5(a). The arrows at the right show spatial distribution of the magnitude of the Poynting vector for this mode.

results were not strongly affected by the assumed value of the real part of the dielectric constant of seawater, and the difference in predicted frequencies was less than 10%.

Figs. 5 and 6 show typical distributions of the electric and magnetic fields in TE and TM modes. Also, arrows at the right show spatial distribution of the magnitude of the

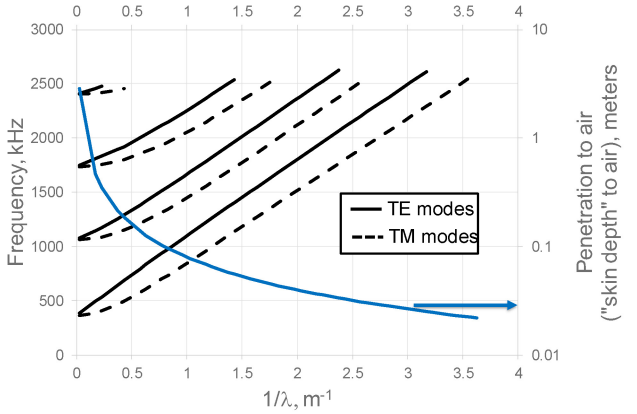

FIGURE 7. Dispersion curves of the TE (solid lines) and the TM (dashed lines) SEW modes calculated for the stratified model shown in Figure 5. The blue curve shows the distance δ_{Air} ("skin depth" into air) above seawater-air interface (d = 20 m).

Poynting vector. As one can see, the TM mode appears to be localized in bulk seawater while the TE mode is localized closer to the seawater-air interface and penetrates high into the air. Thus, the TE mode can be excited by the sources located either above the water or underwater while the TM mode can be excited by the underwater sources only.

Fig. 7 shows dispersion curves of the fundamental and the higher order TE and TM modes calculated for the stratified model shown in Fig. 5. Fig. 7 also presents distance δ_{Air} (the "skin depth" into air) above seawater-air interface, so that the evanescent power above the interface will decay by a factor $e^{-1} = 0.368$ with respect to its value at the interface. The results of these simulations appear to be in agreement with the analytical dependence for the grounded dielectric waveguide [12]:

$$\delta_{Air} = \frac{1}{2\alpha_z} \approx \frac{\lambda_z}{4\pi} \tag{16}$$

where

$$\alpha_z = \sqrt{k_z^2 - \omega^2 \mu_0 \varepsilon_0} \approx k_z \tag{17}$$

This expression is always true (regardless of the actual dielectric constant profile) [13]. For large wave number, the dispersion curve represents themselves equidistant lines similar to the dispersion curves of TE and TM modes of the grounded dielectric waveguide. However, TM modes start bending significantly at smaller wave numbers thus indicating the higher sensitivity of TM mode to the surface condition. To further verify the analytical predictions that TM modes should be more sensitive to the surface conditions, we calculated the dispersion curves for fundamental TE and TM modes in the periodic model shown in the inset of Fig. 8. In this model we assumed that the seawater-air interface is formed by the sinusoidal waves having period D = 50 cm and amplitude of either 25 or 75 cm (peak-peak). Periodic perturbations at the interface lead to the appearance of the Bragg cut-off frequency and additional backward wave branches. This results in multiple splitting

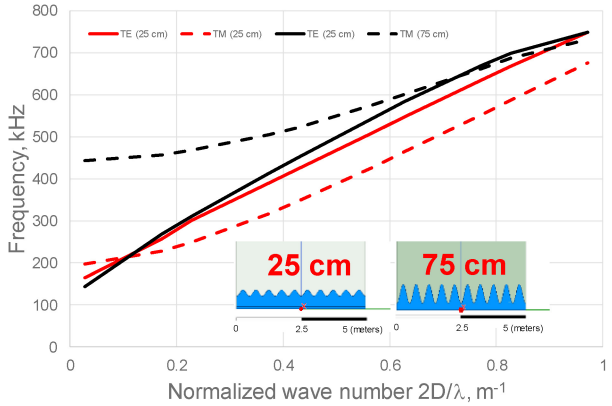

FIGURE 8. Dispersion curves of fundamental TE (solid lines) and TM (dashed lines) SEW modes calculated using periodic Ansys HFSS model shown in the inset. Seawater-air interface is formed by the sinusoidal waves having period D = 50 cm and amplitude d of either 25 or 75 cm (peak-peak).

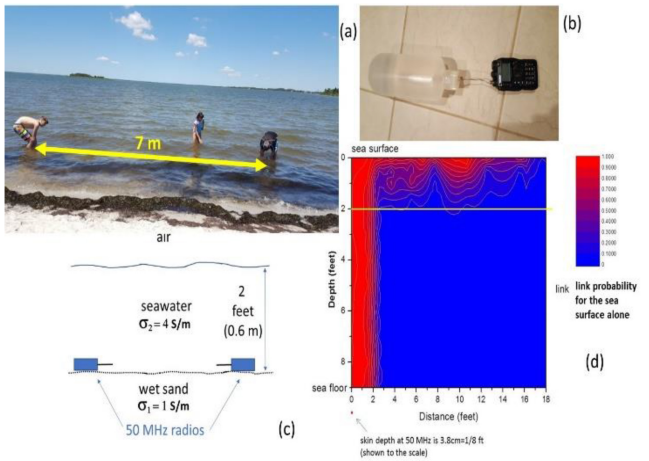

FIGURE 9. (a) Photo of an underwater radio communication experiments using Yaesu VX-8 50 MHz radios equipped with underwater antennas (b) described in detail in [5]. A 50 MHz radio signal was sent along the seabed-seawater interface. The radios were positioned in seawater on the sandy seabed off the Assateague island at a depth of 0.6 m (2 feet), as illustrated in (c). Based on our previous measurements shown in (d) conducted in deep seawater [5], at the 2 feet depth underwater no radio signal associated with a surface wave propagating along the seawater-air interface can be established beyond ~ 4 m distance between the radios. However, in the presence of sandy seabed the communication range of our system extends to about two times larger distances.

of higher order dispersion curves and makes the structure of dispersion curves very complicated. For simplicity, in Fig. 8 we show dispersion curves for the fundamental TM and TE modes only. As one can see, the dispersion curve for the fundamental TE mode does not change much when the amplitude of the waves increases from 5 to 15 meters, while the TM mode shifts up in frequency significantly. It is interesting that for both values of the amplitude the TE and TM curves intersect, thus giving rise to the so called "supersymmetric states" [14].

C. TM WAVE PROPAGATION ALONG THE SEAWATER-SEAFLOOR INTERFACE

Let us now study the TM solutions of Eq. (6) near the seawater-seafloor interface. Based on the measurements reported in [15], the conductivity of sandy seabed may be assumed to be $\sigma = 1$ S/m, which is four times smaller than the average conductivity of seawater $\sigma = 4$ S/m. Therefore, in the ELF/VLF ranges across the boundary of these two media $\varepsilon' << \varepsilon''$, and we may expect $\mathrm{Im}(V) << \mathrm{Re}(V)$ and propagating TM solutions for the effective potential defined by Eq. (6). Indeed, under these circumstances the effective potential in Eq. (6) may be re-written as

$$V = -\frac{i\sigma\omega}{\varepsilon_0 c^2} - \frac{1}{2}\frac{\partial^2\sigma}{\sigma\,\partial z^2} + \frac{3}{4}\frac{(\partial\sigma/\partial z)^2}{\sigma^2} \qquad (18)$$

The behavior of this effective potential in the 10 KHz-50 MHz range has been studied in detail in [8] – see Fig. 2 from [8] and its detailed discussion. Based on this study, the communication distances along the seabed may reach ~ 1500 m at 10 kHz and ~ 10 m at 50 MHz, which far exceed the classical skin depth at the corresponding frequencies. Therefore, compared to the conventional exponentially decaying 3D signal propagation through the lossy bulk seawater, 2D signal propagation along the seawater-seabed interface is highly advantageous.

This prediction appears to be consistent with our experimental observations illustrated in Fig. 9. In these experiments we have used Yaesu VX-8 50 MHz radios equipped with underwater antennas (Fig. 9(c)) which are described in detail in [5]. The radios were positioned in seawater on the sandy seabed off the Assateague island at a depth of 0.6 m (2 feet), as illustrated in Fig. 9(b). Since the electric conductivity of a human body is similar to the conductivity of seawater [16], perturbations caused by the presence of the experimentalists operating the radios underwater appear to be minimal. Based on our previous measurements conducted in deep seawater [5] (see Fig. 9(d)), at the 2 feet depth underwater no radio signal associated with a surface wave propagating along the seawater-air interface can be established beyond ~ 4 m distance between the radios. However, in the presence of sandy seabed the communication range of our system extends to about two times larger distances (as illustrated in Fig. 9(a)).

These experimental results are also consistent with results of our detailed numerical simulations of RF signal propagation along the seawater-seafloor interface. Wave propagation along the seawater-seafloor interface has been simulated with commercial EM solver Altair Feko (version 2021.1) [17]. The stratified conducting media forming such interface have been modelled with planar multilayer lossy dielectric structures. Feko's special Green's function formulation (method of moments extension) implements 2D infinite planes with a finite thickness to model each layer of the dielectric. This simulation approach allows verifying the basic predictions of our theory, and also to illustrate that the wave propagation remains qualitatively the same in a more practical 3D case in contrast to the 1D (planar wave) formulation of our

analytical theory. Seawater layer has been modelled with a 0.58 meter thick dielectric layer with dielectric constant $\varepsilon_r = 81$ and conductivity $\sigma = 4$ S/m. The sand (seafloor) has been modelled as an infinite dielectric layer with $\varepsilon_r = 4$ and conductivity $\sigma = 1$ S/m. Two transition dielectric layers (with thickness of 1 cm each) have been placed between seawater layer and the sand to ensure smooth gradient of conductivity to match real world conditions. These layers had $\varepsilon_r = 81$ and conductivities of 1.1 S/m 1.4 S/m, correspondingly. The infinite dielectric layer having dielectric constant of air has been placed above the seawater layer. Electromagnetic waves have been excited by the point source, namely, by an electric dipole with magnitude of *Idl* = 1 A*m and frequency 50 MHz. This electric dipole has been placed in the center of the lower transition layer well (z = 0) parallel to the seafloor and perpendicular to the observation plane in Fig. 10. Our numerical simulations presented in Fig. 10 confirm that electromagnetic wave can propagate along the seawater-seafloor interface, and that the propagation length of such waves may be considerably larger than the skin depth. As one can see, most of the power propagates along the bottom of the seafloor and just a small fraction of the power leaks into the air. The point source excites simultaneously a volumetric small-k wave (the central circle), attenuating in accordance with the skin depth predictions, and a long propagating large-*k* confined 2D mode which has TM character. The propagation distance of the latter wave is consistent with our experimental measurements illustrated in Fig. 9. We should also note that more numerical and analytical results on electromagnetic wave propagation in strongly lossy multi-layered media (such as, for example, propagation of electromagnetic waves underground) may be found in [18].

D. CURRENT LIMITATIONS AND FUTURE WORK

While the obtained theoretical and experimental results appear to be promising, we should point out several limitations of our current analysis which will be resolved in the future work. As indicated in Section II-B, there are still unsettled issues regarding the true behavior of the dielectric permittivity of seawater in the low frequency ranges. While most theoretical studies assume low frequency behavior depicted by Eq. (9), experimental measurements by Midi et al. [7] cast some doubts on this assumption. A careful dedicated experimental measurement of this behavior is highly necessary.

The currently used analytical model of the $\varepsilon(z)$ behavior in the transition air/water surface layer uses the metamaterial model, which is valid at $\lambda_0 >> D$. Development of an analytical photonic crystal model, which is valid at $\lambda_0 \sim D$ would also be highly desirable. Predictions of such model may be confronted with numerical simulations depicted in Fig. 8.

On the experimental side, careful measurements of communication range as a function of frequency, depth and sea surface waviness would also be highly desirable, since such measurements may be used to validate theoretical results reported here. We are planning to perform such detailed measurements in the future.

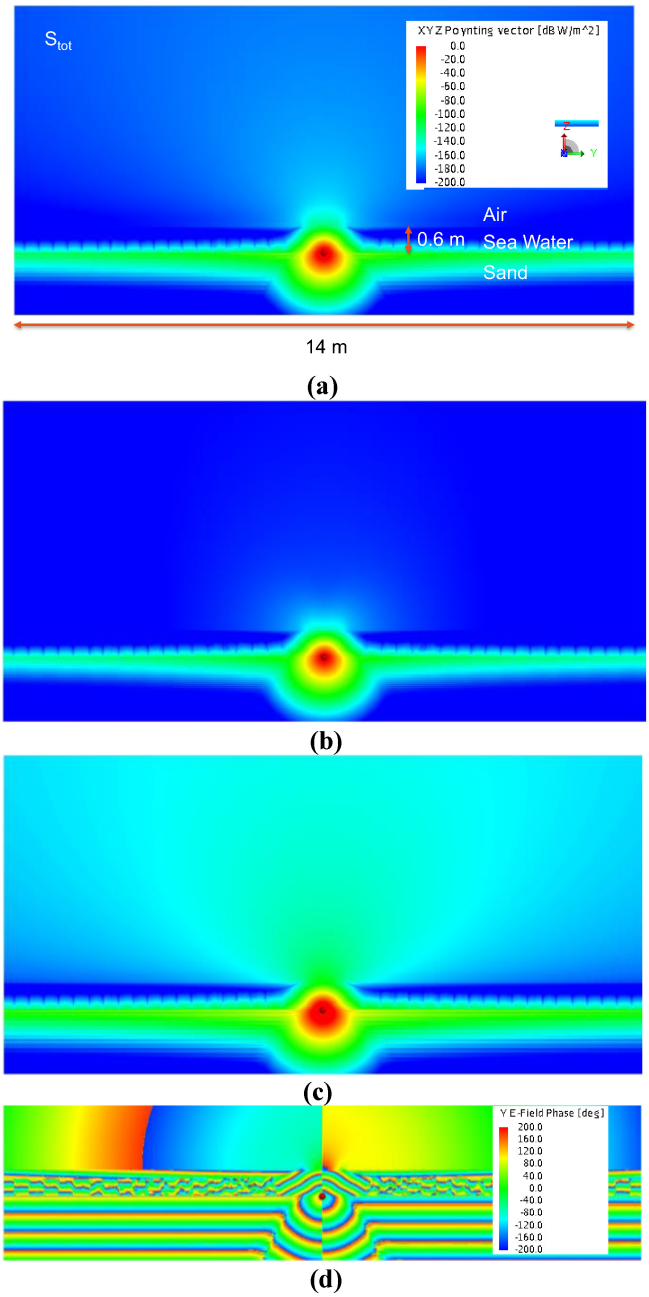

FIGURE 10. Distribution of the magnitude of the Poynting vector (a), magnetic field (b), electric field (c) and instantaneous phase of y-component of the electric field in the TM wave propagating along seawater-seafloor interface

IV. CONCLUSION

In this article we have presented a detailed theoretical and numerical considerations on surface electromagnetic waves propagating along the seawater-air and the seawater-sea floor interfaces and demonstrated experimentally their ability to carry broadband radio signals over practical communication distances underwater. Even though relatively short, these distances would be very useful for physically secure broadband

communication between divers and unmanned underwater vehicles. Compared to acoustic communication, radio communication underwater provides much larger bandwidth. On the other hand, optical wireless communication in turbid seawater may be limited to only a few feet.

Compared to the previous studies reported in [4], [5], [18], where only the properties of TM waves were studied, we also examined the TE-polarized surface wave solutions. It is interesting that the dispersion laws of TE and TM modes may intersect, thus giving rise to the so called "supersymmetric states" [14]. In addition, compared to [5] where only the interface states of the sea surface were studied, we have obtained experimental evidence of 50 MHz radio signal propagation underwater along the sandy seabed.

ACKNOWLEDGMENT

The authors are grateful to V. I. Smolyaninova and A. A. Dema for experimental help.

REFERENCES

[1] R. H. Tyler, T. B. Sanford, and M. J. Unsworth, "Propagation of electromagnetic fields in the coastal ocean with applications to underwater navigation and communication," *Radio Sci.*, vol. 33, pp. 967–987, Jul./Aug. 1998.

[2] X. Che, I. Wells, G. Dickers, P. Kear, and X. Gong, "Re-evaluation of RF electromagnetic communication in underwater sensor networks," *IEEE Commun. Mag.*, vol. 48, no. 12, pp. 143–151, Dec. 2010.

[3] S. Jiang and S. Georgakopoulos, "Electromagnetic wave propagation into fresh water," *J. Electromagn. Anal. Appl.*, vol. 3, pp. 261–266, Jul. 2011.

[4] I. I. Smolyaninov, Q. Balzano, and D. Young, "Surface wave-based radio communication through conductive enclosures," *Progr. Electromagn. Res. M*, vol. 85, pp. 21–28, Sep. 2019.

[5] I. I. Smolyaninov, Q. Balzano, C. C. Davis, and D. Young, "Surface wave based underwater radio communication," *IEEE Antennas Wireless Propag. Lett.*, vol. 17, pp. 2503–2507, 2018.

[6] R. Wangberg, J. Elser, E. E. Narimanov, and V. A. Podolskiy, "Nonmagnetic nanocomposites for optical and infrared negative-refractive-index media," *J. Opt. Soc. Amer. B, Opt. Phys.*, vol. 23, no. 3, pp. 498–505, 2006.

[7] N. S. Midi, K. Sasaki, R. Ohyama, and N. Shinyashiki, "Broadband complex dielectric constants of water and sodium chloride aqueous solutions with different DC conductivities," *IEEJ Trans.*, vol. 9, pp. S8–S12, Oct. 2014.

[8] I. I. Smolyaninov, "Surface electromagnetic waves at gradual interfaces between lossy media," *Progr. Electromagn. Res.*, vol. 170, pp. 177–186, Jun. 2021.

[9] L. D. Landau and E. M. Lifshitz, *Quantum Mechanics*. Burlington, VT, USA: Elsevier, 1977.

[10] B. V. Numerov, "A method of extrapolation of perturbations," *Monthly Notices Roy. Astron. Soc.*, vol. 84, no. 8, pp. 592–601, 1924.

[11] A. V. Zayats, I. I. Smolyaninov, and A. A. Maradudin, "Nano-optics of surface plasmon-polaritons," *Phys. Rep.*, vol. 408, pp. 131–314, Mar. 2005.

[12] K. A. Michalski and J. R. Mosig, "The Sommerfeld half-space problem revisited: From radio frequencies and Zenneck waves to visible light and Fano modes," *J. Electromagn. Waves Appl.*, vol. 30, no. 1, pp. 1–42, 2016.

[13] C. A. Balanis, *Advanced Engineering Electromagnetics*, 2nd ed. Hoboken, NJ, USA: Wiley, 2012.

[14] M. Heinrich et al., "Supersymmetric mode converters," *Nat. Commun.*, vol. 5, p. 3639, Apr. 2014.

[15] H. Müller, T. von Dobeneck, C. Hilgenfeldt, B. SanFilipo, D. Rey, and B. Rubio, "Mapping the magnetic susceptibility and electric conductivity of marine surficial sediments by benthic EM profiling," *Geophysics*, vol. 77, no. 1, p. 1JF-Z19, 2012.

[16] S. B. Baumann, D. R. Wozny, S. K. Kelly, and F. M. Meno, "The electrical conductivity of human cerebrospinal fluid at body temperature," *IEEE Trans. Biomed. Eng.*, vol. 44, no. 3, pp. 220–223, Mar. 1997.

[17] [Online]. Available: www.altair.com/feko

[18] I. I. Smolyaninov and A. B. Kozyrev, "Electromagnetic wave propagation through stratified lossy conductive media," *Progr. Electromagn. Res. M*, vol. 113, pp. 1–10, Aug. 2022.